Simulating space-based observations of orbital debris with PhotSat.

Cinta Isern i Vizoso, Advisor: Josep Manel Carrasco Martínez, Eduard Masana Fresno, Rafael Castillo García, Francesc Vilardell Sallés.

Facultat de Física, Universitat de Barcelona, Martí i Franquès 1, 08028 Barcelona, Spain.
E-mail: cisernvi7@alumnes.ub.edu, carrasco@fqa.ub.edu, emasana@fqa.ub.edu, rcastillo@gmv.com, francesc.vilardell.salles@gmv.com

Abstract: The growing population of artificial objects in Earth orbit has increased the need for effective Space Surveillance and Tracking (SST) capabilities. This work investigates the potential contribution of PhotSat, a 16U CubeSat designed for all-sky photometric monitoring of astrophysical sources, to SST applications as a secondary product of its nominal scientific operations. The artificial space objects expected to cross the PhotSat field of view were simulated over three day survey using a mission simulator developed at the Universitat de Barcelona and the Institut d'Estudis Espacials de Catalunya together with SST simulation software developed by GMV. The resulting observations were analysed according to their orbital and observational characteristics, and their detectability was reassessed using a signal-to-noise ratio (SNR) model that accounts for the apparent magnitude and angular velocity of each object. The results were also compared with simulations of the Telescopi Fabra-ROA Montsec (TFRM), a ground-based optical telescope, performed using the same SST software framework. During the simulated period, 13,721 catalogue objects crossed the PhotSat field of view, of which 12,053 satisfied the nominal SNR ≥ 3 detectability criterion, corresponding to 43.74% of the 27,555 catalogued space objects considered in the simulation. The detectable population was dominated by Low Earth Orbit (LEO) objects, although objects from all the considered orbital regimes were observed. While the most objects are detected only a few times during the three day survey, with a median of 2 detections and a mean of 3.11 detections per object, the results suggest that PhotSat could provide a substantial number of incidental observations of artificial space objects during its nominal survey. These observations could complement those obtained by ground-based SST sensors and potentially contribute to tasks such as observation correlation and orbit determination, although further work based on the analysis of actual PhotSat images will be required to assess their practical applicability.

Resum: El creixement de la població d'objectes artificials en òrbita terrestre ha incrementat la necessitat de disposar de capacitats efectives de vigilància i seguiment espacial (Space Surveillance and Tracking, SST). Aquest treball estudia la possible contribució de PhotSat, un CubeSat de 16U dissenyat per al monitoratge fotomètric de fonts astrofísiques a tot el cel, a aplicacions SST com a producte secundari de les seves operacions científiques nominals.

Es van simular els objectes espacials artificials que s'espera que travessin el camp de visió de PhotSat durant un període de missió de tres dies, mitjançant un simulador de missió desenvolupat a la Universitat de Barcelona i l'Institut d'Estudis Espacials de Catalunya, juntament amb programari de simulació SST desenvolupat per GMV. Les observacions resultants es van analitzar segons les seves característiques orbitals i observacionals, i la seva detectabilitat es va reavaluar mitjançant un model de relació senyal-soroll (SNR) que considera la magnitud aparent i la velocitat angular de cada objecte. Els resultats també es van comparar amb simulacions del Telescopi Fabra-ROA Montsec (TFRM), un telescopi òptic terrestre, realitzades amb el mateix programari SST. Durant el període simulat, 13.721 objectes catalogats van travessar el camp de visió de PhotSat, dels quals 12.053 van satisfer el criteri nominal de detectabilitat SNR $\geq$ 3, corresponents al 43,74% dels 27.555 objectes espacials catalogats considerats en la simulació. La població detectable estava dominada per objectes en òrbita terrestre baixa, tot i que es van observar objectes de tots els règims orbitals considerats. La majoria dels objectes es van detectar poques vegades durant els tres dies, amb una mediana de 2 deteccions i una mitjana de 3,11 per objecte. Els resultats suggereixen que PhotSat podria proporcionar nombroses observacions incidentals d'objectes artificials durant les seves operacions nominals, complementant les observacions dels sensors SST terrestres i contribuint potencialment a tasques de correlació d'observacions i determinació orbital. Tanmateix, caldrà analitzar imatges reals de PhotSat per avaluar-ne l'aplicabilitat pràctica.
KEYWORDS: Space tracking, artificial satellites, simulation, optical astronomy, telescopes, photometry.

Contents

1 Introduction

The increasing dependence of society on satellites for navigation, communications, Earth observation, meteorology, and scientific applications has made the protection of the space environment a critical challenge. The growing number of operational satellites, partly driven by large constellations, contributes to an increasingly populated orbital environment and the accumulation of space debris, increasing the risk of collisions and uncontrolled re-entries. Consequently, monitoring and characterizing the space environment is essential to ensure the safety and sustainability of space activities.

In this context, the concept of Space Situational Awareness (SSA) emerged as the capability to detect, monitor, characterize, and predict objects and events occurring in space that may affect space operations or ground infrastructure. Within the European framework, the European Space Agency (ESA) initiated the SSA programme in 2009, focusing on three main domains: the Space Weather (SWE), the Near-Earth Objects (NEO), and the Space Surveillance and Tracking (SST). SST is specifically devoted to the detection, tracking, cataloguing, and monitoring of artificial objects orbiting the Earth, commonly referred to as Resident Space Objects (RSOs), including active and inactive spacecraft, rocket bodies, and orbital debris.

SST systems maintain and update space-object catalogues to support collision avoidance, fragmentation analysis, and re-entry prediction. SST architectures typically combine distributed sensor networks, including optical telescopes, radars, and laser-ranging stations, with orbit determination and data-processing capabilities. Space objects occupy different orbital regions: LEO extends up to approximately 2,000 km, Medium Earth Orbit (MEO) from approximately 2,000 km to below the geostationary region, and Geostationary Orbit (GEO) lies at approximately 35,786 km. Other relevant regimes include Geostationary Transfer Orbit (GTO), an elliptical trajectory connecting lower altitudes with the geostationary region, and Highly Elliptical Orbit (HEO), spanning a wide altitude range due to its high eccentricity [3]. Optical sensors are mainly employed for MEO, GEO, and HEO, while radars are generally more suitable for LEO.

Since the number of observable objects largely exceeds the available observational resources, the efficient allocation of sensor time is a major challenge. Sensor tasking determines how these resources are allocated under constraints such as field of view, visibility, illumination, and orbital dynamics. Observation strategies are generally divided into survey and tracking modes. Survey observations scan large portions of the sky to detect unknown or uncatalogued objects and support catalogue build-up, whereas tracking observations target known objects to refine their orbital estimates and reduce their associated uncertainties [9, 15].

Parallel to the development of SST capabilities, new space-based astronomical missions are being designed with wide-field survey strategies that could also provide valuable observations of artificial space objects. One of these missions is PhotSat, a 16-unit (16U) CubeSat developed by the Institut d'Estudis Espacials de Catalunya (IEEC) and the Catalan industrial ecosystem. Its primary scientific objective is to perform all-sky photometric monitoring of bright astrophysical sources in the visible and ultraviolet wavelength ranges. Although PhotSat has been conceived for astrophysical observations, its survey strategy makes it an interesting candidate to investigate its potential contribution to SST.

PhotSat is planned to operate in a Sun-synchronous orbit at an altitude of approximately 570 km. The configuration considered in this work corresponds to a dawn-dusk Sun-synchronous orbit (SSO LTAN 06:00), with the spacecraft solar panels maintained perpendicular to the Sun. The exact orbital configuration adopted for the simulations is described in Section 3.2.1.

The satellite payload consists of two small telescopes operating in the visible (VIS) and ultraviolet (UV) wavelength ranges, combined with a rotating mirror mechanism (siderostat). Only the VIS telescope is considered in this work, as SST optical observations rely on reflected sunlight in the visible range and the higher quantum efficiency of the VIS detector enables the detection of fainter objects. The VIS telescope has a focal length of 95.03 mm and an aperture diameter of 57.178 mm, providing a wide field of view of approximately $8^\circ \times 8^\circ$ (11.3° diagonal). Its CMOS detector has a resolution of 2048×2048 pixels, a pixel size of 6.5 μm, and a pixel scale of approximately 14 arcsec/pixel.

The observation strategy is based on maintaining a rigid spacecraft attitude during each orbit while the siderostat scans a great-circle strip across the sky. In the following orbit, the spacecraft is reoriented to modify the siderostat rotation plane, and the process is repeated until the full sky is covered in approximately 2–3 days, excluding a 32° region around the Sun due to Sun-avoidance constraints. The siderostat operates with a nominal step angle of 4°, with each field observed for approximately 50 seconds through 16 frames of 3 seconds, and half of the field being re-observed during the following pointing.

The aim of this project is to investigate the potential of PhotSat for SST applications by studying which artificial space objects could be observed using its nominal survey strategy and comparing its performance with that of a ground-based optical sensor. To this end, simulations are performed using software tools developed by GMV, from which synthetic observations are generated and subsequently analysed.

2 Theoretical background

This section introduces the main concepts governing the observability and optical detectability of artificial space objects, which depend on geometrical conditions and sensor limitations. While some constraints are common to ground- and space-based telescopes, others depend on the telescope location. An object is considered observable when its geometry satisfies the applicable visibility constraints, while detectability determines whether it produces a measurable signal above the optical system's sensitivity threshold.

Several geometrical constraints determine whether an object can be observed. For ground-based telescopes, observations are restricted to night time conditions, defined by a minimum Sun zenith distance to ensure a sufficiently dark sky background. In addition, objects must remain above a minimum elevation to reduce atmospheric effects and avoid obstructions. Space-based telescopes are not affected by these constraints but instead require a minimum angular separation between the field of view and both the Sun and the Earth's limb to avoid detector saturation, stray-light contamination, and Earth occultation. The proximity of the field of view to the Moon or the Galactic plane may also be considered, as their increased background brightness can reduce the signal-to-noise ratio, and some optical sensors therefore impose additional exclusion limits around these regions. In the case of PhotSat, however, no such exclusion limits were considered in the present simulation.

Illumination conditions also play a fundamental role in optical SST observations. Since optical sensors rely on reflected sunlight, the observed object must be illuminated by the Sun and therefore cannot be located within the Earth's umbra or penumbra regions. Consequently, the visibility of an object depends strongly on the relative positions of the Sun, the Earth, the observer and the object.

Once the observability conditions are fulfilled, the detectability of the object mainly depends on its apparent magnitude and the limiting detection magnitude of the telescope.

The apparent magnitude depends primarily on the telescope-object distance, the object size and reflectivity, and the Sun-object-observer phase angle. A formulation commonly used in SST optical observation models for the apparent magnitude of an observed object is given by

$$m_T = m_0 - 2.5 \log_{10} \left(\frac{\frac{2}{3\pi^2} F_{\mathrm{Sun}} \frac{\pi d_s^2}{4R^2} \rho_a \left[\sin\theta + (\pi - \theta)\cos\theta \right]}{F_0} \right), \tag{2.1}$$

where m_T is the apparent magnitude of the object, m_0 is the apparent magnitude of the reference object, F_0 is the flux of the reference object, F_{Sun} is the solar flux, d_s is the characteristic diameter of the object assuming a spherical geometry, R is the distance between the telescope and the object, ρ_a is the geometrical albedo or reflectivity coefficient of the object, and θ is the Sun-object-observer phase angle.

In addition to the apparent magnitude, detectability is commonly expressed in terms of the signal-to-noise ratio (SNR). First, the apparent magnitude of the object is converted into an incoming flux using the expression $F_{\mathrm{obj}} = F_0 10^{-0.4(m_T - m_0)}$. A reference magnitude of $m_0 = 0$ is typically adopted. The corresponding photoelectron rate (S_{obj}) at the detector is then obtained by converting the incident energy flux into photons and accounting for the telescope collecting area,

$$S_{\mathrm{obj}} = F_{\mathrm{obj}} A \frac{\lambda}{hc}, \tag{2.2}$$

where A is the telescope collecting area, λ is the effective wavelength, h is Planck's constant and c is the speed of light. The sky background contribution per pixel (S_{bg}) is computed in the same way from the background magnitude per square arcsecond,

$$S_{\mathrm{bg}} = F_0 10^{-0.4(m_{\mathrm{bg}} - m_0)} A \frac{\lambda}{hc} p^2, \tag{2.3}$$

where m_{bg} is the sky background magnitude per square arcsecond, and p is the angular pixel size.

The resulting SNR is estimated as

$$\mathrm{SNR} = \frac{S_{\mathrm{obj}} Q_e \tau}{\sqrt{S_r + \frac{S_{\mathrm{obj}} Q_e \tau}{N_{\mathrm{pix}}} + (S_{\mathrm{bg}} Q_e + S_d)\, t_{\mathrm{exp}}}}, \tag{2.4}$$

where Q_e is the quantum efficiency, τ is the effective integration time during which the object signal remains within a pixel, S_r is the readout noise variance, S_d is the dark current, t_{exp} is the exposure time, and N_{pix} is the number of pixels over which the object signal is distributed. In this work, $N_{\mathrm{pix}} = 1$.

For moving objects, the effective integration time depends on the apparent angular velocity [14]. If the object crosses a pixel faster than the exposure time, τ is approximated as

$$\tau = \min\left(\frac{p}{\omega}, t_{\mathrm{exp}} \right), \tag{2.5}$$

where ω is the apparent angular velocity of the object. Fast-moving objects therefore produce elongated trails and a reduced SNR, making faint objects more difficult to detect.

For a given SNR threshold, the model can be inverted to obtain the limiting magnitude as a function of angular velocity. This limiting magnitude is then used as the detectability criterion. An object is considered detectable when its apparent magnitude is brighter than the limiting magnitude corresponding to its angular velocity.

3 Methodology

This section describes the simulation tools, setup, and subsequent data processing of the generated data. The main simulation files and data-processing code used in this work are available in a public GitHub repository: https://github.com/cintaa05/PhotSat-SST-TFM.

3.1 Simulation tools

This work relies on four different software tools. Three of them, SENPLANNER, SSTOD and SSDSIM, are commercial off-the-shelf (COTS) software tools developed by GMV for SST applications. The fourth tool is a PhotSat simulator developed by the Universitat de Barcelona and IEEC for the PhotSat mission. Together, these tools form the simulation chain used in this work, from the generation of the satellite pointing strategy to the production of synthetic observations.

Photsat simulator

The PhotSat simulator is a mission simulation tool developed to simulate the expected PhotSat observations, including the generation of the spacecraft pointing strategy and the simulation of synthetic detector images using stellar catalogues, such as Gaia. In this work, only the pointing generation component of the simulator was used to reproduce the all-sky survey strategy described in Section 1 and generate the corresponding observation plan over the selected time interval.

Starting from the orbital configuration, the simulator propagates the satellite orbit and computes the spacecraft attitude throughout the mission. It then determines the telescope line of sight at each observation, producing a time ordered sequence of pointings defined by their observation time, right ascension, and declination.

During the generation of the observation plan, each candidate pointing is evaluated against the spacecraft visibility constraints. Since the solar panels are continuously oriented towards the Sun, the telescope does not point in directions where its field of view would be obstructed by the solar panels. Consequently, the final survey covers almost the entire sky while leaving an exclusion region around the position of the Sun.

The resulting observation plan constitutes the input survey strategy for the SST simulation tools described in the following subsections.

SENPLANNER

The SST Sensor Planner Software (SENPLANNER) from GMV [4] is designed to generate observation schedules and visibility opportunities for networks of SST sensors. It supports optical telescopes, radars, and laser-ranging systems, and provides several execution modes depending on the application, including survey planning, object tracking, and visibility analysis.

The software evaluates the observability of space objects over a user-defined time interval by combining the orbital information of the objects with the sensor characteristics and a set of geometrical and operational constraints. For optical sensors, these constraints are based on the observability criteria described in Section 2 and include, among others, illumination conditions, exclusion angles with respect to the Sun, Moon and Earth's limb, and the sensor field of view. From this analysis, SENPLANNER determines the time intervals during which each object can be successfully observed.

In this work, two execution modes were used. The *Visibility Tracking* (VTRK) and the *Optical Tracking* (OTRK). The VTRK mode computes all visibility intervals for the objects contained in a given catalogue, providing the complete set of observation opportunities independently of telescope scheduling.

The OTRK mode uses these observation opportunities together with the telescope characteristics and operational constraints to generate a feasible observation plan. Since several objects may be simultaneously observable while the telescope can only observe one target at a time, SENPLANNER applies an internal scheduling algorithm to select and optimize the sequence of observations. The resulting plan specifies the object to be tracked at each instant together with the corresponding telescope pointing information, including right ascension, declination, azimuth, and elevation.

SSTOD

The GMV SST Orbit Determination software (SSTOD) [5] includes several execution modes for orbit determination and propagation, Two-Line Element (TLE) estimation and fitting, track correlation, catalogue processing and orbit analysis. The software is based on the ESA NAPEOS orbit determination and propagation engine [2].

Among the available execution modes, only the `TLEP` mode was used in this work. This mode propagates an input TLE over the simulation interval and generates a binary orbit file containing the resulting spacecraft ephemeris. This file provides the time-dependent position of the space-based sensor in the format required by the subsequent simulation software.

SSDSIM

SSDSIM is the SST Sensor Data Simulator software developed by GMV [6]. It simulates observations acquired by sensor networks, including optical telescopes, radars, satellite laser ranging stations, and passive ranging sensors. Its main objective is to simulate the observations that would be acquired by a given sensor from a population of RSOs, allowing the performance of different SST sensors and survey strategies to be assessed.

Starting from a catalogue of RSO, the sensor characteristics, and an observation strategy, SSDSIM propagates the object population orbits over the simulation interval and evaluates their observability according to the geometrical constraints described in Section 2. For each sensor pointing, the software determines which objects lie within the field of view and satisfy the observation conditions. The generated outputs include the observable objects together with parameters such as apparent magnitude, phase angle, angular velocity, and radial distance. SSDSIM was the main simulation tool used to evaluate the potential of PhotSat for SST.

3.2 Simulation setup

This section describes the simulation setup for the two considered scenarios: PhotSat and the Telescopi Fabra-ROA Montsec (TFRM), used as a representative ground-based optical sensor. TFRM is a robotic 0.5-m Baker-Nunn telescope located at the Montsec Astronomical Observatory, with a field of view of approximately $4.4° \times 4.4°$ [13]. The main sensor parameters adopted for both scenarios are summarized in Appendix A.

3.2.1 PhotSat simulation

The first step of the simulation consisted of generating the PhotSat pointing sequence using the Photsat simulator described in Section 3.1. The simulation was configured through an XML file containing the reference epoch, orbital parameters, and survey characteristics, including the telescope field of view and angular scanning pattern.

The simulations were performed over a three day interval, from 21 to 24 June 2025. The starting date was selected according to the availability of the auxiliary Earth-orientation and space-environment data required by the GMV software, described later in this section. The RSO population used in the simulation comprised 27,555 real Earth-orbiting objects obtained from a catalogue available in the GMV operational environment and catalogued at the beginning of the analysed interval, representing the known population available from this source at that time. The three day duration was chosen because the generated pointing sequence showed that the nominal PhotSat survey achieves complete sky coverage within this interval, as illustrated in Figure 1. The small uncovered region corresponds to the Sun exclusion zone described in Sec. 1.

For the selected interval, the simulator produced a chronological sequence of telescope pointings, specifying the observation epoch and the right ascension and declination of the telescope line of sight. Since SSDSIM does not directly read the original simulator output, the sequence was reformatted into the telescope survey format accepted by SSDSIM, where each entry defines the pointing time interval and coordinates.

In addition to the pointing history, SSDSIM requires the time dependent position of the space-based sensor in a compatible binary orbit format. For this reason, the PhotSat orbit was propagated with SSTOD using its `TLEP` execution mode. For the simulations, the nominal LTAN 06:00 orbital configuration was adopted, with an altitude of approximately 570 km, an inclination of 97.58°, an eccentricity of 0.0005, an argument of perigee and mean anomaly of 0°, a Right Ascension of the Acending Node (RAAN) of 0°, and a mean motion of 15.011 rev/day. Since PhotSat has not yet been launched, no operational TLE is available, therefore, a representative TLE was constructed from these parameters using 21 June 2025 as its reference epoch. SSTOD propagated this TLE over the simulation interval and generated the binary orbit file, which provides the spacecraft ephemeris required by SSDSIM. The complete TLE used in the simulation is provided in Appendix B.1.

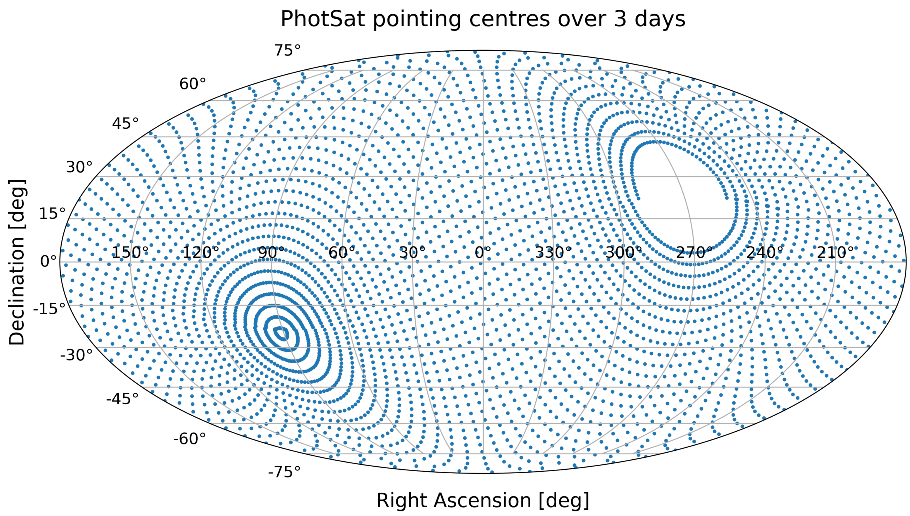

Figure 1. Distributions of the PhotSat pointing centres (blue points) over the celestial sphere after three days of simulated observations, shown in a Mollweide projection.

The PhotSat VIS telescope was defined in the SSDSIM sensor database and linked to the spacecraft orbit through its carrier identifier. The sensor configuration includes the observation duration, field of view, and the geometrical constraints used to determine observability, including the minimum angular separation from the Sun, the Earth-limb grazing angle, the minimum distance from the Galactic plane, and the accepted angular-velocity and radial-distance ranges (see Appendix A).

The database also defines operational parameters such as the slew time, minimum passage duration, and expected sensor success rate, and links the sensor to auxiliary functions describing the Moon exclusion constraint, limiting magnitude as a function of angular velocity, and measurement accuracy. Parameters associated with a fixed terrestrial location are not applicable to PhotSat.

The RSO catalogue contains the TLEs of the objects described above, identified by their NORAD catalogue numbers. A common albedo value was assigned to all objects for the computation of their apparent magnitudes, while no additional filtering by orbital regime was applied before the simulation.

The general SSDSIM execution was controlled through the `config.dat` and `expert_config.dat` files. These define the simulated sensor and object population, propagation settings, dynamical models, and generated products. Most advanced perturbation options available in the expert configuration were kept at their default or disabled values.

Both SSTOD and SSDSIM additionally require auxiliary Earth-orientation, time-scale, and space-environment data. The same datasets were used in both tools to maintain a consistent propagation setup. The IERS Earth Orientation Parameters (`finals2000A.data`), TAI–UTC leap-second data (`tai-utc.dat`), and daily solar and geomagnetic activity (RSGA) files covering 2025, obtained from the IERS/CDDIS and NOAA archives [7, 8, 12]. These data provide the reference-frame transformations, time-scale conversions, and space-environment indices required by the propagation models.

Together, the telescope survey, the PhotSat binary orbit, the RSO catalogue, the sensor database, the execution configuration and the auxiliary environmental files define the complete set of inputs required by SSDSIM to reproduce the PhotSat observation scenario.

The main SSDSIM outputs used in the analysis were the visibility file (`visibilities.dat`), the object catalogue (`ObjectCatalogue.dat`), and the midpoint events file (`midpoint.dat`). The first contains the visibility intervals obtained for each object, while the second provides the physical and orbital properties associated with the simulated population. The main dataset analysed in this work was `midpoint.dat`, which contains one entry per simulated detection, including the observation epoch, sensor and object identifiers, apparent magnitude, angular velocity with respect to the observing sensor, phase angle, and radial distance. The structure and relevant fields of these output files are described in Appendix B.2.

In addition to the physical quantities, the `midpoint.dat` file also provides the margins with respect to the limiting magnitude and maximum angular velocity defined for the sensor. In the adopted SSDSIM configuration, potential detections were initially filtered using a limiting magnitude of 19 and a maximum angular velocity of 10 $\deg s^{-1}$. However, the subsequent analysis did not rely on these simplified thresholds, and detectability was instead reassessed using the SNR criterion described in Section 2, which provides a more realistic limiting magnitude as a function of the object's angular velocity.

3.2.2 TFRM simulation

The TFRM analysis covered the same period from 21 to 24 June 2025. Unlike PhotSat, whose pointing sequence was generated from its nominal survey strategy, TFRM was analysed using SENPLANNER. The same RSO catalogue and auxiliary data described for the PhotSat simulation were used, while no spacecraft orbit file was required because TFRM is a ground-based sensor. Its configuration was already available in the internal SENPLANNER and SSDSIM sensor databases.

SENPLANNER was primarily executed in VTRK mode to compute all observation opportunities satisfying the TFRM visibility constraints for every object in the catalogue. Since VTRK does not perform scheduling optimization, its output may contain simultaneous visibility intervals that cannot all be observed in practice. Nevertheless, it provides the complete set of potentially observable objects and was therefore used to compare the apparent magnitudes obtained from TFRM with those obtained from PhotSat, independently of telescope scheduling.

OTRK mode was additionally used to generate a feasible observation schedule by selecting a non-overlapping subset of the available observation opportunities according to the SENPLANNER optimization criteria. Each opportunity slot is assigned an optimization value according to configurable scheduling rules that consider factors such as object priority and required update rate, the available observation opportunities, and sensor characteristics such as limiting magnitude and slew time. The highest-ranked opportunities are then selected while avoiding simultaneous observations. In this case, the scheduling strategy is also oriented towards distant objects, particularly the GEO population. The resulting `Schedule_TF21RM24.dat` file specifies the observation intervals and target objects, while the `ObjectElevAzim_TF21RM23.dat` file provides the corresponding telescope pointing information, including right ascension, declination, elevation, and azimuth. Together, these outputs were used to generate the telescope pointing history required by SSDSIM.

The generated pointing history was provided to SSDSIM together with the same RSO catalogue, auxiliary data, and execution configuration used for the PhotSat simulation. The resulting `midpoint.dat`, `visibilities.dat`, and `ObjectCatalogue.dat` files were used as an additional comparison with the PhotSat results.

The complete simulation workflows for the PhotSat and TFRM scenarios are summarized in Figure 2.

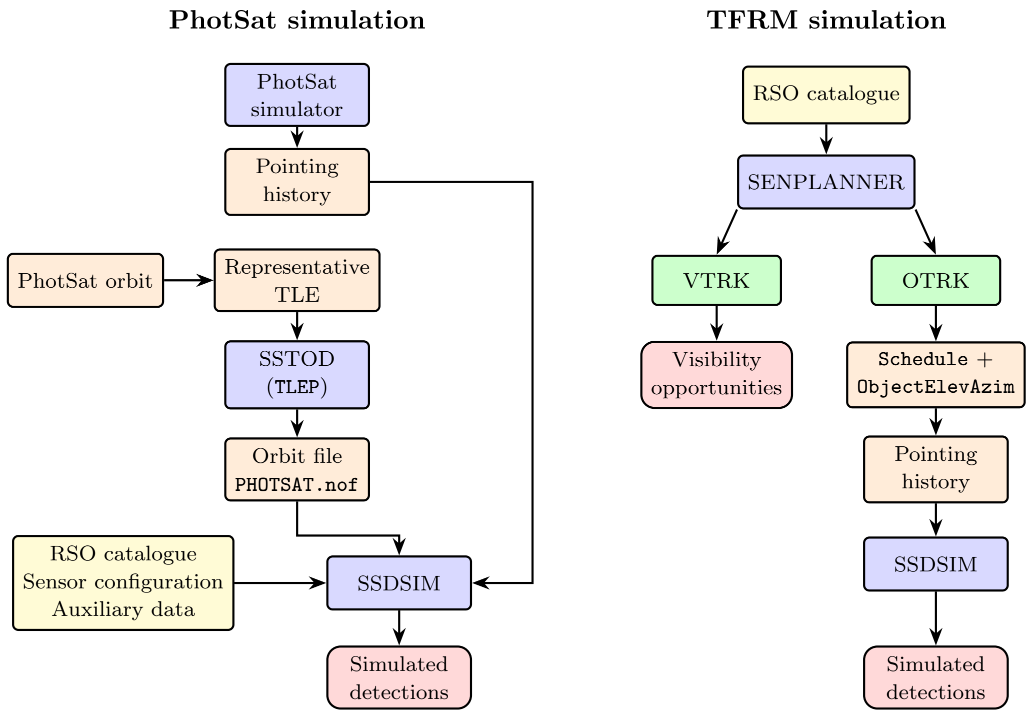

Figure 2. Simulation workflows for the PhotSat and TFRM observation scenarios. For PhotSat, the pointing history and spacecraft orbit are generated using the PhotSat simulator and SSTOD, respectively, and provided to SSDSIM. For TFRM, SENPLANNER VTRK provides the complete set of visibility opportunities, while OTRK generates the observation schedule used to construct the pointing history provided to SSDSIM.

3.3 Processing of the data

The SSDSIM outputs were processed by enriching the simulated detections with additional orbital and physical information, classifying the objects by orbital regime, and applying the SNR-based detectability criterion described in Section 2.

3.3.1 Construction of the enriched catalogue

To enable a more comprehensive analysis of the simulated observations, the information associated with each detection was complemented with additional physical and orbital properties. This was achieved by combining the `midpoint.dat` file produced by SSDSIM with the corresponding `ObjectCatalogue.dat` file and with the public satellite catalogue distributed by CelesTrak, using the NORAD catalogue number as the common identifier. Descriptions of the CelesTrak catalogue structure and the resulting enriched dataset are provided in Appendix B.3.

The CelesTrak catalogue provides one entry for each catalogued Earth-orbiting object and contains updated identification, physical and orbital information, including the object name, international designator, object type, operational status, ownership, launch date, orbital period, inclination, perigee and apogee altitudes, and radar cross section. Since this catalogue is regularly maintained and represents the most up-to-date source of information, its values were adopted whenever available. The information contained in the `ObjectCatalogue.dat` file was only used to complete parameters that were not available in the external catalogue.

As part of the enrichment process, each object was assigned to one of six orbital classes: LEO, MEO, GEO, GTO, HEO and Others, the latter grouping objects that did not satisfy the criteria of any of the defined orbital classes or for which the required orbital information was incomplete. The classification was applied sequentially according to the criteria summarized in Table 1. It was primarily based on the perigee altitude (h_p) and apogee altitude (h_a), allowing the identification of the LEO, GEO, GTO and MEO populations.

For the remaining objects, the orbital eccentricity was additionally computed as

$$e = \frac{r_a - r_p}{r_a + r_p}, \tag{3.1}$$

where $r_p = R_E + h_p$ and $r_a = R_E + h_a$, with r_p and r_a denoting the perigee and apogee distances from the Earth's centre, respectively, h_p and h_a the corresponding perigee and apogee altitudes, and R_E the Earth's mean radius. Objects that were not classified in the previous groups were assigned to the HEO population when $e \geq 0.5$ and $h_a > 20000$ km. All remaining cases, including objects with incomplete orbital information, were grouped into the *Others* category. This mainly includes objects in intermediate or crossing orbits that fall outside the adopted class boundaries, such as objects with LEO perigees but apogees above 2000 km that do not satisfy the GTO or HEO criteria, as well as high-altitude or geosynchronous orbits outside the adopted GEO range.

Table 1. Criteria adopted to classify the detected objects according to their orbital regime. Here h_p and h_a denote the perigee and apogee altitudes, respectively.

Orbit class	**Classification criterion**
LEO	$h_a < 2000$ km
GEO	$h_p \geq 33786$ km and $h_a \leq 37786$ km
GTO	$h_p < 2000$ km and $30000 \leq h_a \leq 45000$ km
MEO	$h_p \geq 2000$ km and $h_a < 33786$ km
HEO	Not classified above, $e \geq 0.5$ and $h_a \geq 20000$ km
Others	Remaining cases or missing orbital information

3.3.2 Detectability filtering

Although the detections generated by SSDSIM already satisfy the simplified limiting magnitude and angular velocity thresholds defined for the sensor, their detectability was reassessed using the SNR model presented in Section 2. Two detection thresholds were considered. SNR ≥ 3 was adopted as the nominal detection limit, consistent with its common use as a minimum criterion for optical source detection [10], while SNR ≥ 6 was considered a more conservative criterion to assess the sensitivity of the results to a stricter detection requirement. For each observation, the limiting magnitude corresponding to its angular velocity was obtained from the calculated SNR curve, and only observations brighter than this limit were retained.

This procedure generated three datasets for each sensor. The complete set of detections provided by SSDSIM, the detections satisfying SNR ≥ 3, and those satisfying SNR ≥ 6. These datasets were subsequently used throughout the results section to analyse the detectability of the simulated observations.

4 Results

This section presents the results obtained from the simulations described in the previous section and evaluates the potential use of PhotSat for SST. The analysis focuses on the fraction and characteristics of the space object population that can be detected during the telescope survey, taking into account the adopted SNR criteria. The properties and temporal characteristics of the resulting observations are also examined. Results obtained for the TFRM ground based telescope are included where relevant to provide a reference for the performance of PhotSat and to highlight differences between the two strategies.

4.1 Overall detection

The overall detection performance was analysed by considering the observations generated for PhotSat during the 3 day simulation. Figure 3 shows the apparent magnitude and angular speed of the simulated observations, with the objects classified according to the orbital regimes defined in Section 3.3.1. The limiting curves corresponding to SNR $= 3$ and SNR $= 6$, calculated using the detectability model described in Section 2, are also included.

A clear dependence on the orbital regime can be observed. LEO objects (in blue) generally present highest relative angular speeds, while GEO objects are concentrated at considerably lower angular speeds and generally fainter magnitudes (as expected due to their larger distances). MEO, GTO and HEO objects occupy intermediate regions of the magnitude-angular speed space. Figure 3 also illustrates the dependence of the detection limit on the angular motion of the object. As the angular speed increases, the object spends less time within each pixel, reducing the signal collected during its passage and consequently requiring a brighter magnitude to reach the same SNR. Observations located below each curve, corresponding to apparent magnitudes brighter than the limiting value for a given angular speed, satisfy the respective SNR detection criterion. Therefore, the

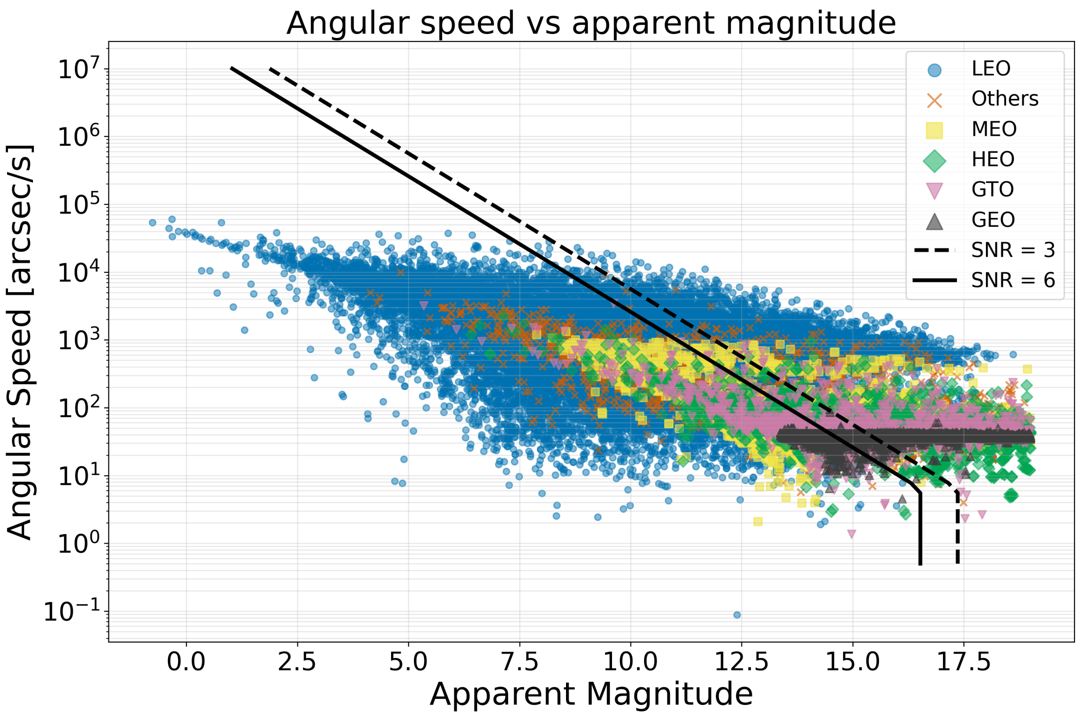

Figure 3. Apparent magnitude and angular speed of the objects observed by PhotSat during the simulated period, classified according to their orbital regimes. The black dashed and continuous curves represent the limiting magnitude as a function of angular speed for SNR = 3 and SNR = 6, respectively.

region below the dashed curve corresponds to observations with SNR $\geq$ 3, while the region below the continuous curve corresponds to the more restrictive SNR $\geq$ 6 criterion.

Table 2 summarizes the detections and unique objects before and after applying the SNR thresholds. Of the 27,555 catalogue objects, 49.79% were observed, decreasing to 43.74% for SNR $\geq$ 3 and 40.51% for SNR $\geq$ 6. Nevertheless, 92.6% of the objects detectable at SNR $\geq$ 3 remain detectable at SNR $\geq$ 6.

Table 2. Summary of the observations obtained for PhotSat and TFRM during the three-day simulation. The percentage is calculated with respect to the 27,555 objects in the input catalogue.

Sensor	**Criterion**	**Detections**	**Unique objects**	**Catalogue (%)**
PhotSat	SSDSIM output	49,703	13,721	49.79
	SNR $\geq$ 3	37,476	12,053	43.74
	SNR $\geq$ 6	32,962	11,162	40.51
TFRM	SSDSIM output	7,420	1,326	4.81
	SNR $\geq$ 3	7,400	1,320	4.79
	SNR $\geq$ 6	7,387	1,316	4.78

In contrast, almost all observations included in the TFRM schedule satisfy both SNR criteria, resulting in only a negligible reduction in both detections and unique objects after SNR filtering. However, the resulting values remain considerably lower than those obtained with PhotSat.

The difference in the number of objects observed by the two sensors must be interpreted considering their different observation strategies. The visibility analysis performed for TFRM identified 66,104 potential observation opportunities, corresponding to approximately 15,806 different objects. However, many of these opportunities overlap in time and cannot be observed simultaneously by a single telescope. Besides, the observation activities from ground-based observatories must be stopped during daylight, reducing considerably its availability for SST programmes. Consequently, the optimized schedule generated by SENPLANNER resulted in simulated observations of 1,326 unique objects. In contrast, the PhotSat survey allowed 13,721 different catalogue objects to cross the telescope field of view within only three days, of which 12,053 satisfied the SNR ≥ 3 criterion. Although these results do not represent a direct comparison of the intrinsic performance of the two telescopes, they highlight one of the main advantages of the PhotSat survey for SST applications. Its ability to provide observations of a large number of different space objects over a relatively short period while performing its nominal survey operations.

4.2 Characterization of the detectable population

The distribution of the detectable objects among the different orbital populations is summarized in Table 3. The PhotSat population is strongly dominated by LEO objects, within 9,081 unique objects satisfying SNR ≥ 3 and 8,743 satisfying SNR ≥ 6. However, this predominance largely reflects the composition of the input catalogue, in which LEO objects represent approximately 83% of the classified population. When the number of detected objects is compared with the total catalogue population of each orbital class, the fraction of objects satisfying SNR ≥ 3 ranges from 39.52% for LEO to 80.46% for MEO, showing that PhotSat provides detectable observations across all the considered orbital regimes.

The orbital distribution obtained for TFRM differs considerably from that of PhotSat, with GEO objects constituting its largest detected population. However, since the main objective of this work is to characterize the SST capabilities of PhotSat, the following analysis focuses on the PhotSat observations satisfying SNR ≥ 3.

Table 3. Number and fraction of unique catalogue objects detected by PhotSat and TFRM for each orbital population after applying the SNR criteria. Percentages are calculated relative to the total number of objects of each orbital class in the input catalogue.

	Catalogue	**PhotSat**		**TFRM**	
Orbit	**objects**	**SNR** ≥ 3	**SNR** ≥ 6	**SNR** ≥ 3	**SNR** ≥ 6
LEO	22979	9081 (39.52%)	8743 (38.05%)	179 (0.78%)	179 (0.78%)
MEO	609	490 (80.46%)	422 (69.29%)	121 (19.87%)	119 (19.54%)
GEO	1629	1103 (67.71%)	843 (51.75%)	468 (28.73%)	468 (28.73%)
GTO	616	325 (52.76%)	261 (42.37%)	186 (30.19%)	185 (30.03%)
HEO	573	311 (54.28%)	247 (43.11%)	143 (24.96%)	142 (24.78%)
Others	1149	743 (64.66%)	646 (56.22%)	223 (19.41%)	223 (19.41%)

Figure 4 shows the apparent magnitude, radial distance and estimated diameter distributions of the detectable PhotSat population. The apparent magnitudes cover a broad range, with most detections between approximately magnitudes 5 and 15[1]. The overall distribution presents a broad maximum around magnitude 10 and a secondary concentration around magnitude 13–14. As discussed below, this structure results from the superposition of orbital populations with different magnitude distributions.

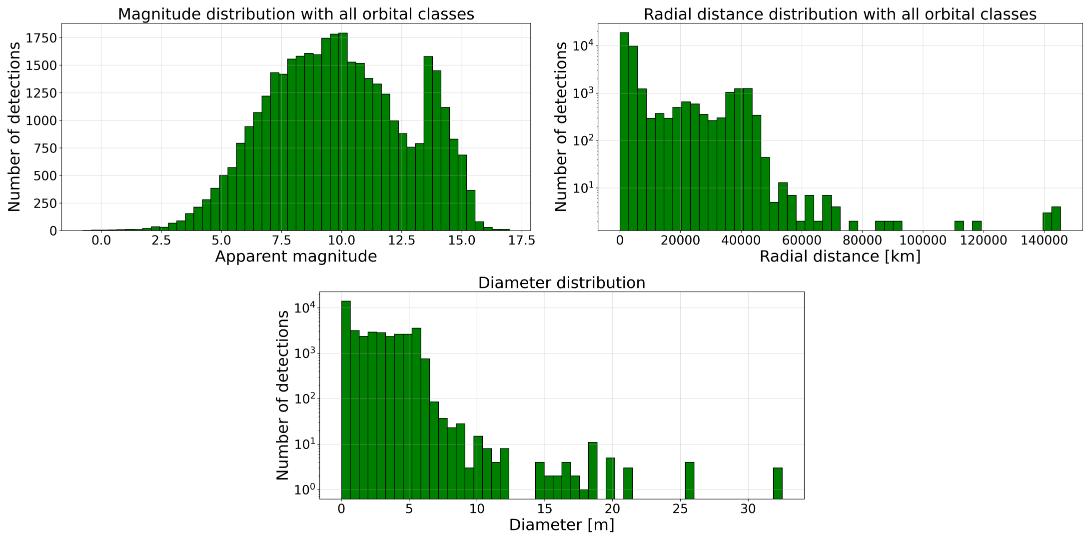

Figure 4. Distribution of the apparent magnitude (top left), radial distance from PhotSat to the satellite (top right), and estimated diameter (bottom) of the PhotSat detectable population for SNR ≥ 3. Magnitude and radial distance are represented per detection, while diameter is represented per unique object.

The distribution of the radial distance from PhotSat to the satellites is strongly concentrated at relatively short distances, mainly due to the predominance of LEO objects, although detectable observations are obtained at distances extending beyond 10^5 km. The estimated diameter distribution is dominated by relatively small objects, with a tail towards larger sizes. These values should be interpreted as approximate catalogue-based estimates.

The magnitude distributions separated by orbital population, shown in Figure 5, explain the structure observed in the overall distribution and illustrate the effect of the SNR criterion on each population. LEO objects, which dominate the detected population, are generally brighter, with most detections concentrated between approximately magnitudes 5 and 12, while GEO objects are concentrated at fainter magnitudes, mainly between 13.5 and 15.5, contributing to the secondary peak observed in the overall distribution. MEO, GTO and HEO objects generally occupy intermediate-to-faint magnitude ranges, while the Others category presents a broader distribution. The SNR criterion preferentially removes faint observations, with the detectable LEO population limited to approximately magnitude 12.5 compared with around magnitude 15 for the other populations. This is mainly due to the higher angular velocities of LEO objects, which reduce the effective integration

[1] Although the PhotSat VIS detector saturates for objects brighter than approximately magnitude 9, its CMOS detector does not exhibit blooming, allowing the position of saturated objects to still be determined.

time and require brighter objects to reach the same SNR, as illustrated in Figure 3.

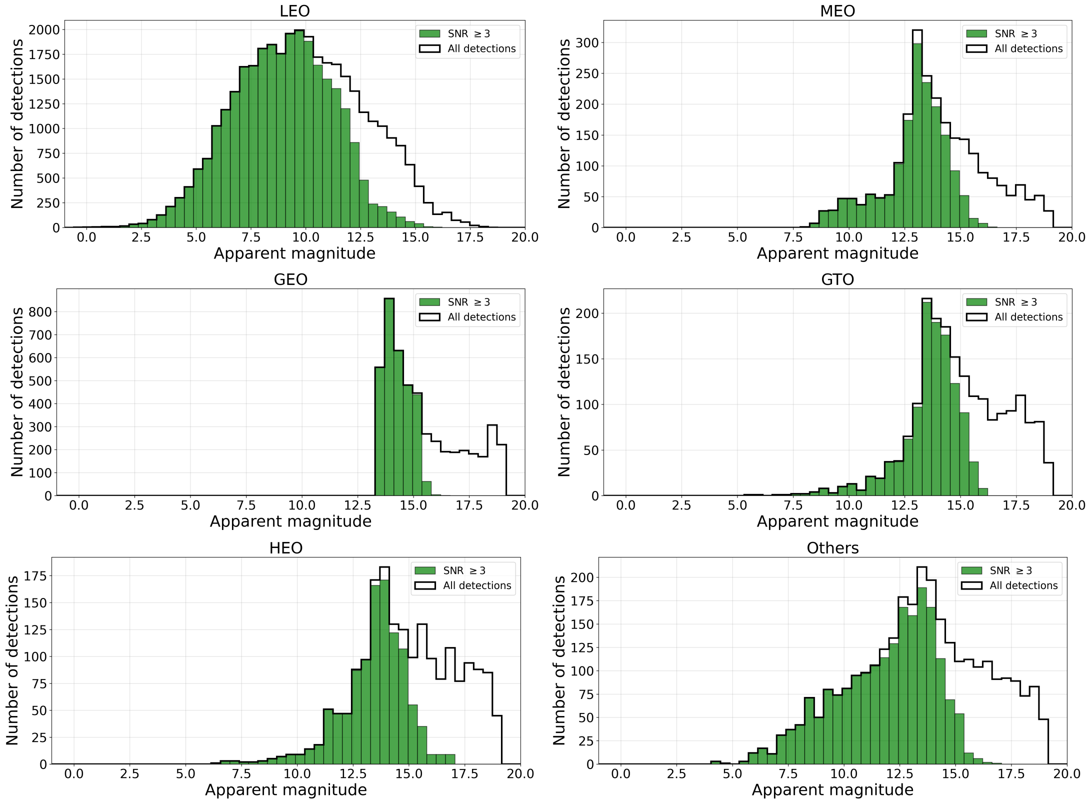

Figure 5. Apparent magnitude distributions of PhotSat observations separated by orbital population. The black outline represents all simulated observations crossing the PhotSat field of view, while the green histograms show those satisfying SNR ≥ 3.

The radial-distance distributions, shown in Figure 6, further illustrate the different orbital regions sampled by PhotSat and the effect of the detectability criterion as a function of distance. LEO observations are concentrated at the shortest distances, whereas MEO and GEO detections occur predominantly at several tens of thousands of kilometers. GTO and HEO objects span wider distance ranges as a consequence of their eccentric trajectories, with HEO observations extending beyond 10^5 km. The heterogeneous Others population also spans a wide range of distances. Therefore, despite the strong numerical predominance of LEO objects, PhotSat provides detectable observations across all the considered orbital regimes and over a broad range of distances.

4.3 Observation characteristics

In addition to the number and characteristics of the detectable objects, the amount of observational information obtained for each object was analysed. Figure 7 compares the number of detections per object and the duration of continuous visibility intervals obtained for PhotSat and TFRM.

For PhotSat, the 37,476 detections satisfying SNR ≥ 3 correspond to 12,053 unique objects. The number of detections per object ranges from 1 to 36, with a mean of 3.11

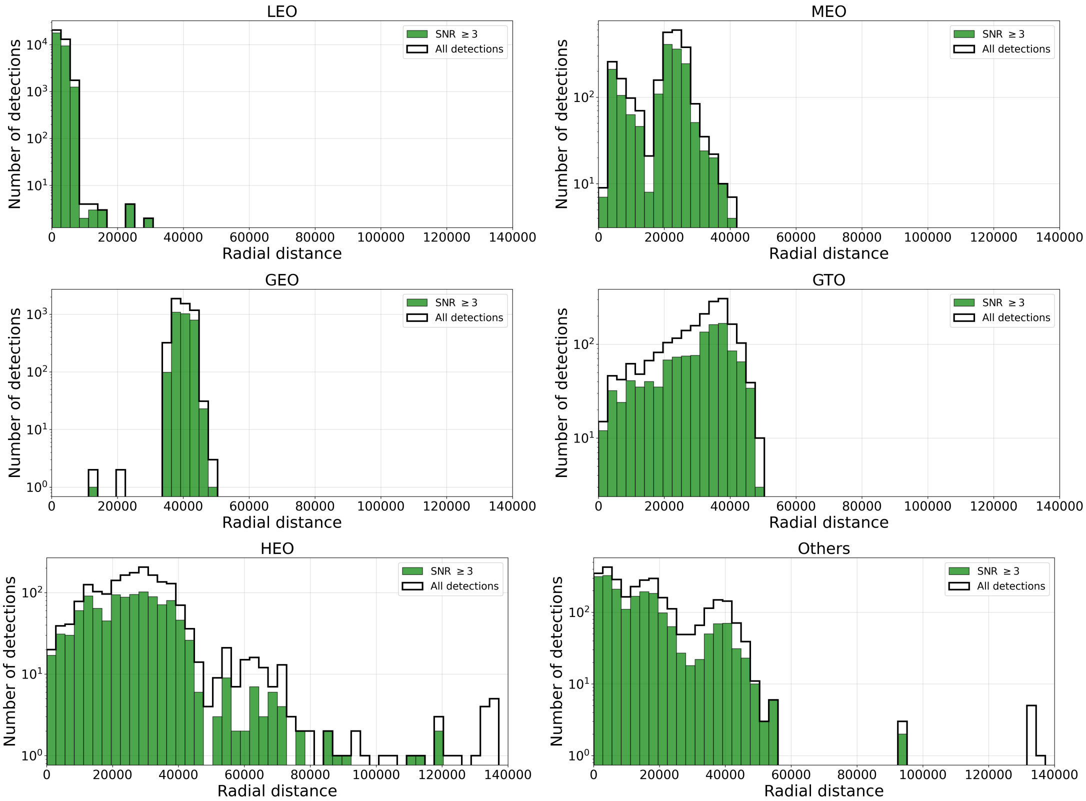

Figure 6. Radial-distance distributions of PhotSat observations separated by orbital population. The black outline represents all simulated observations crossing the PhotSat field of view, while the green histograms show those satisfying SNR ≥ 3.

and a median of 2. Most objects are therefore detected only a few times during the three-day survey, although a smaller fraction is observed repeatedly. In particular, 75% of the detected objects present up to four detections and 90% up to six.

For TFRM, the 7,400 detections satisfying the same SNR criterion correspond to 1,320 unique objects, with a mean of 5.61 and a median of 3 detections per object. The distribution extends up to 61 detections for a single object, indicating a higher number of repeated observations for some targets.

The continuous visibility intervals present similar characteristic durations for both sensors. PhotSat produced intervals, with a mean duration of 0.67 min and a median of 0.39 min, while TFRM produced 5,804 intervals, with a mean of 0.63 min and a median of 0.50 min. The longest intervals reached 6.81 min and 7.50 min for PhotSat and TFRM, respectively. These intervals represent continuous visibility within the sensor field of view, rather than continuous tracking or continuous detectability above the adopted SNR threshold.

These results must, however, be interpreted considering the fundamentally different observation strategies. TFRM observations are scheduled to observe selected known objects, whereas PhotSat detections occur incidentally when space objects cross the telescope field of view during its nominal survey operations. Consequently, the higher number of repeated detections per object obtained for TFRM does not imply a better survey capability. In

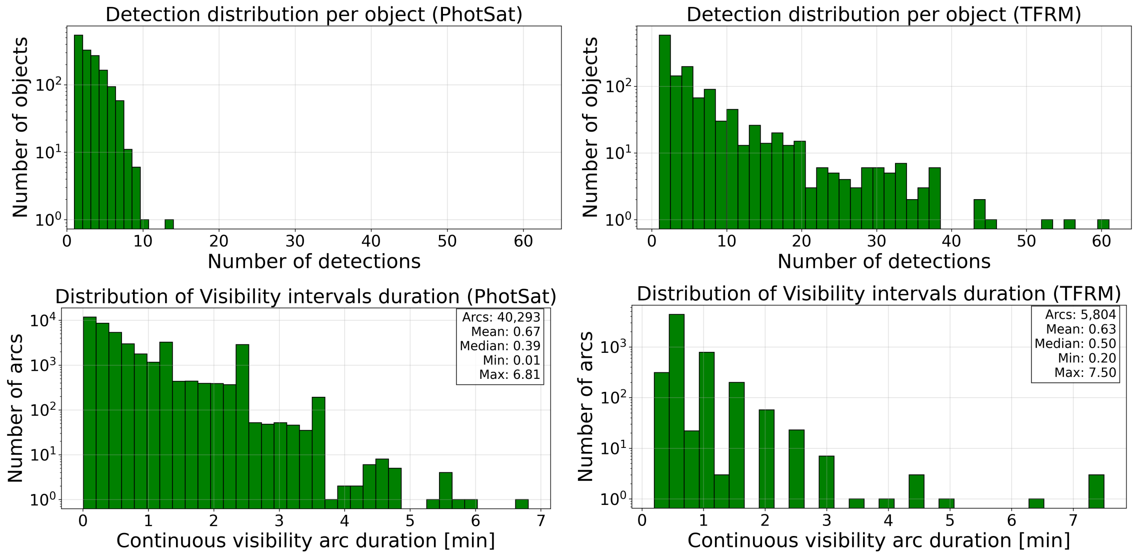

Figure 7. Observation characteristics obtained for PhotSat (left) and TFRM (right). The upper panels show the number of detections per unique object satisfying SNR $\geq$ 3, while the lower panels show the duration of the continuous visibility arcs obtained from the corresponding visibility intervals.

contrast, PhotSat provides observations of a much larger number of different objects without dedicated SST scheduling. The repeated detections and visibility arcs obtained during the survey may nevertheless provide useful information for observation correlation and subsequent orbit determination, including for objects that cannot be targeted in advance.

4.4 Comparision with ground-based observations

Finally, the apparent magnitudes obtained with PhotSat and TFRM were compared for objects observed by both sensors. Two TFRM datasets were considered: all potential observation opportunities obtained with VTRK and the subset included in the optimized SENPLANNER schedule and simulated with SSDSIM. While VTRK identifies all potential observation opportunities from TFRM, the schedule determines which can actually be performed. For each common object, the brightest observed magnitude was selected for each sensor, and the magnitude difference was defined as

$$\Delta m = m_{\mathrm{TFRM}} - m_{\mathrm{PhotSat}}, \tag{4.1}$$

such that positive values indicate that the object is observed at a brighter apparent magnitude by PhotSat.

Figure 8 shows the resulting distributions. When considering all TFRM visibility opportunities, 6,991 objects were common to both datasets. PhotSat provided the brighter observation for 64.9% of these objects, with a mean magnitude gain of 0.87 mag and a median of 0.99 mag. This indicates that, for a substantial fraction of the objects potentially visible from TFRM, the PhotSat observation geometry can result in a brighter apparent magnitude.

In contrast, when the comparison is restricted to the optimized TFRM schedule, 867 objects are common to both simulations and the magnitude difference becomes nearly centred around zero. PhotSat provides the brighter observation for 42.7% of the common objects, while TFRM does so for 57.3%, with a mean magnitude difference of only −0.006 mag and a median of −0.084 mag.

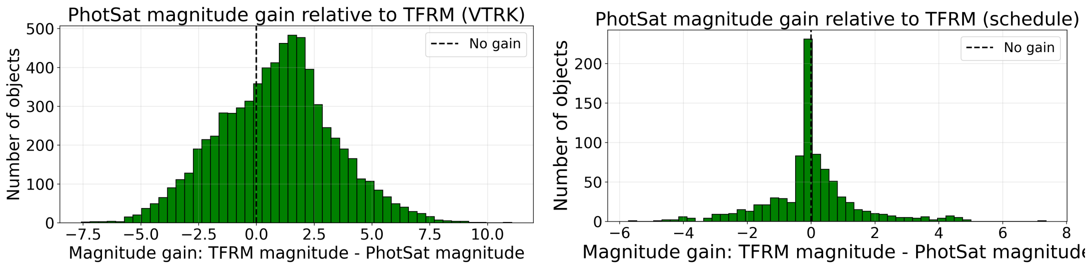

Figure 8. Distribution of the difference between the best apparent magnitude obtained with TFRM and PhotSat for common objects. The left panel considers all potential TFRM observation opportunities obtained with VTRK, whereas the right panel uses only the feasible observations selected by the SENPLANNER schedule and subsequently simulated with SSDSIM. Positive values correspond to objects observed at a brighter magnitude by PhotSat.

The difference between the two distributions reflects their different object populations. Of the 6,991 objects common to PhotSat and the complete TFRM visibility dataset, the population is dominated by LEO objects, which account for 75.1%, while GEO objects represent only 4.5%. In contrast, among the 867 objects common to PhotSat and the optimized TFRM schedule, the LEO contribution decreases to 12.8%, while GEO objects become the most represented orbital population, accounting for 31.1%. This change is consistent with the TFRM survey strategy implemented by SENPLANNER, which selects a feasible set of observations from the available visibility opportunities and is oriented towards surveying the GEO region. The resulting schedule therefore provides TFRM with favourable observation opportunities for a substantially different orbital population, helping to explain why the magnitude difference becomes nearly centred around zero.

The comparison therefore highlights the complementary characteristics of the two observing strategies. Apparent magnitude depends on the instantaneous observation geometry, including sensor–object distance and phase angle, which differ between space- and ground-based observers. While the optimized TFRM schedule provides targeted observations selected from the available visibility opportunities, the PhotSat all-sky survey obtains favourable observation geometries for a large number of objects without dedicated SST scheduling. The results thus illustrate the potential of PhotSat to complement targeted ground-based observations across different orbital populations.

5 Conclusions

This work studied the potential contribution of PhotSat to SST applications by simulating the artificial space objects observable during its nominal survey. The main result is that, despite not being designed as an SST mission, PhotSat is expected to observe a substantial number of artificial objects during its scientific operations.

During the three-day simulated survey, 13,721 different catalogue objects crossed the PhotSat field of view. After applying the SNR-based detectability model, 12,053 objects remained detectable for SNR $\geq$ 3, corresponding to 43.74% of the 27,555 objects in the input catalogue within only three days of survey operation. Even for the more restrictive SNR $\geq$ 6 criterion, 11,162 objects remained detectable. The detectable population is strongly dominated by LEO objects. Overall, these results indicate that artificial-object detections are expected to be a frequent occurrence during PhotSat operations rather than isolated events.

The survey also provides repeated observations of some objects. For the SNR $\geq$ 3 population, objects were detected on average 3.11 times, with a median of two detections, while continuous visibility arcs had a median duration of approximately 0.39 min. Although these observations are generally short and are obtained without dedicated SST scheduling, they may provide useful information for observation correlation and subsequent orbit determination. This could be particularly relevant for objects that have not yet been identified or correlated with an existing catalogue entry.

The comparison with TFRM illustrates the complementary nature of space- and ground-based observations. While TFRM can perform targeted tracking of selected objects, PhotSat can observe a much larger number of different objects incidentally during its survey. Moreover, a space-based telescope is not restricted to night-time operation or affected by atmospheric and weather conditions, although its observations remain subject to geometrical and illumination constraints. PhotSat could therefore provide complementary observations from a different location and geometry to those obtained by existing ground-based SST sensors.

Finally, the results should be interpreted considering the population included in the simulation. The analysis used an input catalogue containing 27,555 objects representative of the catalogued population in 2025, whereas PhotSat is expected to be launched in 2027. Since the number of catalogued objects continues to increase and is already substantially larger than the population considered here, the orbital population available by the expected PhotSat launch in 2027 may be considerably larger. Moreover, the simulations could only reproduce observations of objects already included in the input catalogue and therefore, did not account for unknown or uncatalogued objects that may also cross the PhotSat field of view. Consequently, the number of artificial objects potentially observed by PhotSat during its operational lifetime could be significantly larger than represented in this study, although their effective detectability will depend on their physical properties and observation geometry.

Overall, this study demonstrates that PhotSat has significant potential to provide valuable SST observations as a secondary product of its astrophysical mission. Future work should assess the identification and correlation of artificial objects directly from PhotSat images and determine whether the resulting observations can support initial orbit determination and catalogue maintenance, providing a more complete assessment of the potential integration of PhotSat data into existing SST systems.

Acknowledgments

I would first like to express my gratitude to my supervisors, Josep Manel Carrasco and Eduard Masana, for giving me the opportunity to take part in this project and to carry out the Master's Thesis in collaboration with GMV. I am very grateful for their guidance, support, and availability throughout the project, and for all their help whenever I needed it. I would also like to thank GMV for giving me the opportunity to join the company as an intern and for trusting me with this project. In particular, I would like to thank Rafael Castillo, who has guided me throughout the project and provided me with the tools, knowledge, and support necessary to carry out this work. I am also specially grateful to Francesc Vilardell, who has been my main point reference at the Barcelona office of GMV.

Finally, I would like to thank my family for their constant support and encouragement. I am also especially grateful to the friends I have met during the Master's degree, who have made this journey not only academically enriching, but also a much more enjoyable and memorable experience.

A Sensor parameters used in the simulations

Table 4 summarizes the main parameters adopted for the PhotSat VIS telescope and TFRM in the simulations and in the SNR-based detectability analysis. Only the parameters relevant to the present study are included.

Table 4. Main sensor parameters adopted for the PhotSat VIS telescope and TFRM in the simulations and SNR-based detectability analysis.

Parameter	**PhotSat VIS**	**TFRM**
Field of view	$8° \times 8°$	4.41°
Detector resolution	2048×2048 pixels	4096×4096 pixels
Pixel size	6.5 μm	9.0 μm
Pixel scale	14 arcsec/pixel	3.9 arcsec/pixel
Focal length	95.03 mm	480 mm
Aperture diameter	57.178 mm	500 mm
Observation duration (SSDSIM)	0.052 min	6 min
Exposure time (SNR model)	3.125 s	30 s
Effective wavelength	542 nm	542 nm
Quantum efficiency	0.95	0.60
Readout noise	1.6 e^-	9 e^-
Dark current	0.07 e^- s^{-1}	0.07 e^- s^{-1}
Minimum Sun distance / Sun zenith distance	4°	105°
Minimum Galactic-plane distance	0°	1°
Grazing angle / cut-off elevation	0°	15°
Maximum angular speed	10 deg s^{-1}	2 deg s^{-1}
Radial-distance constraint	None	None
Mean slew time	1.7 s	1.7 s
Minimum dwell time	0.5 s	12 s

B Simulation and data-processing files

B.1 PhotSat representative TLE

Since PhotSat had not yet been launched at the time of this study, a representative TLE was constructed from the nominal orbital parameters adopted in the simulation. The TLE used as input to the SSTOD `TLEP` propagation, with a reference epoch of 21 June 2025, was:

```
PHOTSAT
1 99999U 27001A   25172.00000000  .00000000  00000-0  00000-0 0  9992
2 99999  97.5800   0.0000 0005000   0.0000   0.0000 15.01100000    09
```

B.2 SSDSIM output files

The main SSDSIM outputs used in the analysis were the `visibilities.dat`, `ObjectCatalogue.dat`, and `midpoint.dat` files. The following sections provide a brief description and representative examples of their structure.

midpoint.dat

The `midpoint.dat` file is an additional SSDSIM output containing one entry for each simulated observation event, evaluated at the midpoint of the corresponding visibility interval. This file constituted the main input dataset for the subsequent analysis. Its fields are summarized in Table 5.

Table 5. Fields contained in the `midpoint.dat` file.

Field	Description
Epoch	Epoch corresponding to the observation event
Sensor ID	Identifier of the observing sensor
Object ID	Identifier of the observed object
True angular speed	Apparent angular speed of the object
Angular speed	Margin with respect to the configured maximum angular speed
Sun distance	Angular separation between the line of sight and the Sun
Minimum GP distance	Angular distance to the Galactic plane
Minimum Moon distance	Angular separation from the Moon
Radial distance	Distance between the sensor and the observed object
True magnitude	Simulated apparent magnitude of the object
Magnitude	Margin with respect to the configured limiting magnitude
Phase angle	Sun–object–observer phase angle

Despite their names, the *Magnitude* and *Angular Speed* fields do not correspond to the physical apparent magnitude and angular speed of the object. The actual simulated quantities are stored in *True Magnitude* and *True Angular Speed*, respectively. The other two fields represent the corresponding margins with respect to the simplified sensor thresholds configured in SSDSIM. In the adopted PhotSat configuration, these thresholds were a limiting magnitude of 19 and a maximum angular speed of 10 $\deg\,s^{-1}$. For example, an entry with a true magnitude of 11.62 has a magnitude margin of 7.38 with respect to the configured limiting magnitude of 19. Similarly, a true angular speed of 0.0416 $\deg s^{-1}$ corresponds to a remaining margin of approximately 9.9584 $\deg s^{-1}$ with respect to the configured 10 $\deg s^{-1}$ limit.

visibilities.dat

The `visibilities.dat` file contains the time intervals during which an object satisfies the visibility conditions of the survey sensor and remains within its field of view. Each entry identifies the beginning and end of the visibility interval, the sensor and its carrier, the observed object, and the associated measurement accuracy.

Table 6. Main fields contained in the `visibilities.dat` file.

Field	Description
Visibility start time	Beginning of the visibility interval
Visibility end time	End of the visibility interval
Sensor ID	Identifier of the observing sensor
Carrier ID	Identifier of the platform carrying the sensor
Object ID	Identifier of the observed object
Population group ID	Population group associated with the object
Mean accuracy	Mean angular measurement accuracy during the interval

ObjectCatalogue.dat

The `ObjectCatalogue.dat` file contains the physical and orbital properties associated with the object population generated or ingested by SSDSIM. Although the complete file contains additional information used internally by the software, only a subset of its fields was relevant to the analysis performed in this work. These included the object identifier, COSPAR identifier, estimated diameter and area, radar cross section, albedo, orbital period, orbital regime, and Keplerian orbital elements.

Table 7. Main `ObjectCatalogue.dat` fields used in the analysis.

Field	Description
Object ID	Internal/NORAD object identifier
COSPAR ID	International designator of the object
Diameter	Estimated equivalent spherical diameter
Area	Object area adopted by the simulation
RCS	Radar cross section
Albedo	Optical albedo adopted for magnitude computation
Orbital period	Orbital period of the object
Orbital regime	Orbital-class information provided by SSDSIM
Semimajor axis	Keplerian semimajor axis
Eccentricity	Keplerian orbital eccentricity
Inclination	Keplerian orbital inclination
RAAN	Right ascension of the ascending node
Argument of perigee	Keplerian argument of perigee
True anomaly	Keplerian true anomaly

B.3 External catalogue and enriched dataset

CelesTrak satellite catalogue

The public CelesTrak SATCAT catalogue was used to complement the information available in the SSDSIM object catalogue. The catalogue was linked to the simulated detections through the NORAD catalogue identifier. The main fields used in the enrichment process are summarized in Table 8.

Table 8. Main CelesTrak SATCAT fields used to enrich the simulated detections.

Field	Description
OBJECT_NAME	Object name
OBJECT_ID	International/COSPAR designator
NORAD_CAT_ID	NORAD catalogue identifier
OBJECT_TYPE	Payload, rocket body, or debris classification
OPS_STATUS_CODE	Operational status code
OWNER	Object owner or launching organization
LAUNCH_DATE	Launch date
DECAY_DATE	Orbital decay date, when applicable
PERIOD	Orbital period
INCLINATION	Orbital inclination
APOGEE	Apogee altitude
PERIGEE	Perigee altitude
RCS	Radar cross section
ORBIT_TYPE	Orbit status/type reported in the catalogue

Enriched detection catalogue

The final dataset used for the analysis was constructed by combining each detection in the `midpoint.dat` file with the information available in `ObjectCatalogue.dat` and the CelesTrak SATCAT catalogue. The NORAD catalogue identifier was used as the primary key to associate the detections with the corresponding catalogue entries. When available, information from SATCAT was prioritized, while `ObjectCatalogue.dat` was used to complement missing information.

The resulting enriched catalogue therefore combines the observational quantities provided by SSDSIM with identification, physical, and orbital information for each detected object. It also includes quantities derived during the processing, such as the angular speed expressed in arcsec s^{-1} and the orbital class assigned according to the criteria described in Section 3.3.1. The complete set of fields contained in the final enriched catalogue is shown in Table 9.

Table 9. Fields contained in the enriched detection catalogue used for the analysis.

Field	Source	Description
DateTime	midpoint	Observation epoch
DateTime_raw	midpoint	Original epoch string
SensorID	midpoint	Identifier of the observing sensor
ObjectID	midpoint	Object identifier in the simulation
NORAD_ID	SATCAT / SSDSIM	NORAD catalogue identifier
COSPAR_ID	SATCAT / SSDSIM	International designator
ObjectName	SATCAT	Object name
ObjectType	SATCAT	Object type
OperationalStatusCode	SATCAT	Operational status code
OperationalStatus	Derived	Interpreted operational status
Active	Derived	Flag identifying active objects
Owner	SATCAT	Owner or launching organization
LaunchDate	SATCAT	Launch date
DecayDate	SATCAT	Decay date, when applicable
TrueMagnitude	midpoint	Simulated apparent magnitude
Magnitude	midpoint	Margin with respect to the limiting magnitude
TrueAngularSpeed	midpoint	Simulated apparent angular speed
TrueAngularSpeed_arcsec_s	Derived	Angular speed converted to arcsec s^{-1}
AngularSpeed	midpoint	Margin with respect to the maximum angular speed
RadialDistance	midpoint	Sensor-to-object distance
PhaseAngle	midpoint	Sun–object–observer phase angle
CosSunDistance	midpoint	Angular separation from the Sun
MinimumGPDistance	midpoint	Minimum angular distance to the Galactic plane
MinimumMoonDistance	midpoint	Minimum angular distance to the Moon
Perigee	SATCAT	Perigee altitude
Apogee	SATCAT	Apogee altitude
Inclination	SATCAT	Orbital inclination
Eccentricity	Derived	Orbital eccentricity
Period	SATCAT	Orbital period
OrbitClass	Derived	Orbital class assigned in this work
OrbitType_satcat	SATCAT	Orbit type provided by SATCAT
Diameter	SSDSIM	Estimated object diameter
Area	SSDSIM	Object area
RCS	SATCAT / SSDSIM	Radar cross section

References

[1] J. M. Carrasco, I. Esteva, C. Sierra-Roig, G. Anglada-Escudé, and I. Ribas, *The PhotSat mission: Ultraviolet and visible all-sky monitoring with a CubeSat*, 2025.

[2] European Space Agency, *NAPEOS: Mathematical Models and Algorithms*, Technical Note DOPS-SYS-TN-0100-OPS-GN, Version 1.0, ESOC, 2009.

[3] European Space Agency (ESA), "Types of orbits," ESA. Available online: https://www.esa.int/Enabling_Support/Space_Transportation/Types_of_orbits (accessed July 2026).

[4] GMV, *SENPLANNER: SST Sensor Scheduling and Tasking Software*, available at: https://www.gmv.com/es/docs/software-planificacion-tareas-sensores-sst/senplanner, accessed July 2026.

[5] GMV, *Ecosstm: Space Surveillance and Tracking Software Suite*, available at: https://www.gmv.com/es-es/productos/espacio/ecosstmr, accessed July 2026.

[6] GMV, *SSDSIM: SST Sensor Data Simulation*, available at:

https://www.gmv.com/en/docs/sst-sensor-data-simulation/ssdsim, accessed July 2026.

[7] International Earth Rotation and Reference Systems Service (IERS), *Earth Orientation Parameters: finals2000A.data*, NASA Crustal Dynamics Data Information System (CDDIS). https://cddis.nasa.gov/archive/products/iers/finals2000A.data.

[8] International Earth Rotation and Reference Systems Service (IERS), *TAI–UTC Time Scale Data: tai-utc.dat*, NASA Crustal Dynamics Data Information System (CDDIS). https://cddis.nasa.gov/archive/products/iers/tai-utc.dat.

[9] Richard Linares and Roberto Furfaro, *An Autonomous Sensor Tasking Approach for Large Scale Space Object Cataloging*, (2017).

[10] M. J. Mazur, S. Metchev, R. A. Brown, R. Gupta, R. Bloch, T. Mills, and E. Pass, "The Colibri Telescope Array for KBO Detection through Serendipitous Stellar Occultations: A Technical Description," *Frontiers in Astronomy and Space Sciences*, vol. 9, Art. no. 929573, 2022, doi: 10.3389/fspas.2022.929573.

[11] Alessandro Mignocchi, Sebastian Samuele Rizzuto, Alessia De Riz, and Marco Felice Montaruli, *Advanced Sensor Tasking Strategies for Space Object Cataloging*, Sensors **26**, (2026).

[12] National Oceanic and Atmospheric Administration (NOAA), *Reports of Solar and Geophysical Activity*, National Centers for Environmental Information. https://www.ngdc.noaa.gov/stp/spaceweather/swpcproducts/daily_reports/reports_solar_geophysical_activity/.

[13] Observatori Fabra, *The Fabra-ROA Telescope at the Montsec (TFRM)*, available at: https://observatorifabra.cat/astronomy/the-fabra-roa-telescope-at-the-montsec-tfrm/?lang=en, (accessed June 2026).

[14] Thomas Schildknecht, *Optical Astrometry of Fast Moving Objects Using CCD Detectors*, Geodätisch-geophysikalische Arbeiten in der Schweiz, Vol. 49, Schweizerische Geodätische Kommission, 1994.

[15] Chenbao Xue, Han Cai, Steve Gehly, Moriba Jah, and Jingrui Zhang, *Review of sensor tasking methods in Space Situational Awareness*, (2024).